Link between optical spectra, crystal-field parameters, and local environments of Eu^{3+} ions in Eu_2O_3-doped sodium disilicate glass

T. Qin,[1,*] G. Mountjoy,[1] N. D. Afify,[1,†] M. F. Reid,[2] Y. Y. Yeung,[3] A. Speghini,[4] and M. Bettinelli[4]

[1]*School of Physical Sciences, University of Kent, Canterbury CT2 7NH, United Kingdom*

[2]*Department of Physics and Astronomy and MacDiarmid Institute for Advanced Materials and Nanotechnology, University of Canterbury, Christchurch 8140, New Zealand*

[3]*Department of Science and Environmental Studies, The Hong Kong Institute of Education, 10 Lo Ping Road, Tai Po, New Territories, Hong Kong, China*

[4]*Laboratorio di Chimica dello Stato Solido, DB, Università di Verona, INSTM, UdR Verona, I-37134 Verona, Italy*

(Received 14 January 2011; revised manuscript received 14 June 2011; published 13 September 2011)

Rare-earth-doped glasses are key materials for optical technology due to the luminescent properties of $4f^n$ ions. The crystal-field model describes the effect of local environment on transitions between $4f$ electrons. We present a detailed modeling study of the optical spectra of sodium disilicate glass, $33Na_2O \cdot 67SiO_2$, doped with 0.2% and 1.0 mol% Eu_2O_3. This study uses very large molecular dynamics models with up to 100 Eu^{3+} ions, the superposition model for covalent and overlap effects on crystal-field parameters, and realistic values for homogeneous linewidth broadening. The simulated spectra are in reasonable agreement with experiment. The trends in ^7F_J energy levels across different Eu^{3+} ion sites have been examined and a very detailed analysis is presented that looks at how features of the spectra are related to features of the local environment of Eu^{3+} ions. Increasing the crystal-field strength S_{total} causes the $^7F_0$ energy level to decrease and causes the splitting of ^7F_J manifolds to increase, and this is due to increasing mixing of $4f$ wave functions. To a reasonable approximation the crystal-field strength components S_k depend on angular positions of ligands independently of distances to ligands. The former are seen to be more significant in determining S_k, which are closely related to the rotationally invariant bond-orientational order parameters Q_k. The values of S_2 are approximately linear in Q_2, and the values of Q_2 are higher for fivefold than sixfold coordinated rare-earth ions. These results can be of importance for efforts to enhance the local environment of rare-earth ions in oxide glasses for optical applications.

DOI: 10.1103/PhysRevB.84.104206 PACS number(s): 78.20.Bh, 78.55.Qr, 81.05.Kf, 78.60.Lc

I. INTRODUCTION

Glasses containing rare-earth ions have been widely studied for applications such as lasers and optical fiber amplifiers. Glasses have a great advantage over crystalline systems, since they can be easily prepared at high quality and with a range of chemical compositions.[1] The luminescent properties of these glasses are directly related to the $4f$-$4f$ transitions of the rare-earth ions. The energy levels of rare-earth $4f$ electrons can be predicted by solving the Hamiltonian that describes the interactions which the $4f$ electrons experience. The energy levels are described using labels $^{2S+1}L_J$, where S, L, and J are the quantum numbers of spin, orbital angular momentum, and total angular momentum for the wave function of the $4f$ electrons. The Eu^{3+} ions are known as excellent optical probes because the ground state $^7F_0$ and the first excited state $^5D_0$ are nondegenerate and well separated.[2] Figure 1 schematically shows the energy absorption and emission diagram of the Eu^{3+} ion.

The purpose of the present paper is to carry out a detailed modeling study of the link between the optical spectra and the local environment of Eu^{3+} ions in a glass. The glass chosen for this study is Eu_2O_3-doped sodium disilicate glass $33Na_2O \cdot 67SiO_2$ because this glass has been well studied using structural techniques, and reliable molecular dynamics potentials exist. In addition, the optical spectra of this glass have previously been reported.[4]

Crystal-field theory can be used to calculate the energy levels for each individual Eu^{3+} ion. In previous studies the crystal-field calculations were frequently made using the point charge electrostatic model (PCEM).[5] The PCEM assumes that interactions between the Eu^{3+} ions and the ligand ions are purely electrostatic. As a result, the short-range covalent and overlap interactions are ignored, which is not physically sound.[6] The superposition model (SM) that takes into account all these interactions has proved to be more realistic.[6–9] Previously, the superposition model has often been applied for crystal structures in which the rare-earth environment is described using a particular symmetry group.[6] In this paper the superposition model is applied to glass structures without assuming any symmetry.

The Eu^{3+} ion energy levels can be calculated from the crystal-field theory using parameters obtained from the superposition model. Similarly, the parameters to calculate the transition probability between energy levels and, hence, intensities can also be obtained from the superposition model. The superposition model for the transition probability has only been used for high symmetry crystal structures previously,[10] and in this paper it will be used for glass structures for the first time.

The shapes of transition lines in the spectra are broadened according to two main mechanisms: homogeneous and inhomogeneous broadening.[11] For the homogeneous broadening mechanism, all the individual Eu^{3+} ions are assumed to experience a lifetime broadening, and for the inhomogeneous broadening mechanism, the individual Eu^{3+} ions experience different local environments and thus contribute to different parts of the spectra. The homogeneous broadening is described

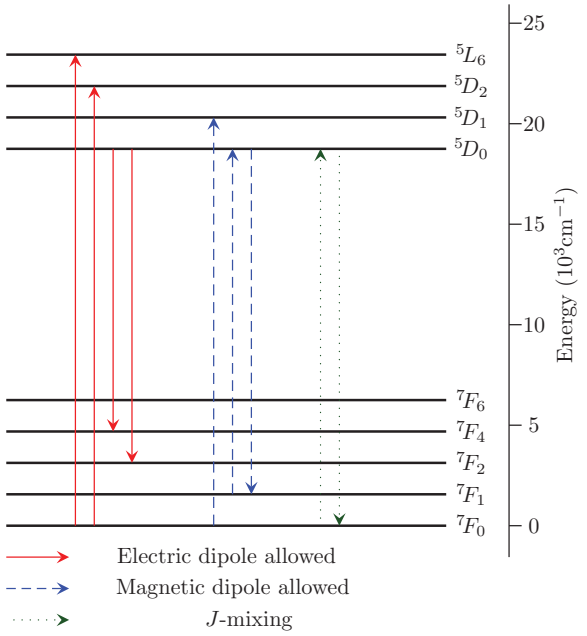

FIG. 1. (Color online) Schematic illustration of optical transitions of the Eu^{3+} ion.[3] The frequently observed absorption and emission transitions are indicated.

using the Lorentzian profile, and the inhomogeneous broadening is often approximated using a Gaussian profile. The present study will use the molecular dynamics results to obtain inhomogeneous broadening by summing up the different Eu^{3+} local environments so there is no need for approximating it using a Gaussian profile.

A method to obtain the optical spectra of europium-doped glass from molecular dynamics results was previously presented in 1993.[4,12] The final spectra in that paper were generated by summing up the contributions from all the 150 Eu^{3+} ions, and a Gaussian profile was also added to give additional broadening.[4]

In general, it is preferable to demonstrate a comprehensive, straightforward, and sensible methodology to obtain the optical spectra, which is the first aim of this paper. The calculated results also enable us to investigate how the local environment of the Eu^{3+} ions influences the associated luminescence features, which is the second aim of this paper.

The paper will be organized in the following manner. In Sec. II, the details of the molecular dynamic simulations will be presented together with brief structural results for models of europium-doped sodium disilicate glasses. Two models of 0.2mol% and 1mol% Eu_2O_3-doped sodium disilicate ($33Na_2O \cdot 66SiO_2$) glass are generated with approximately 15 000 atoms each. In Sec. III, the superposition model will be used to calculate the crystal-field parameters, and then crystal-field theory will be used to calculate the energy levels of individual Eu^{3+} ions. The transition probability between different energy levels is also calculated via the superposition model. By applying the homogeneous broadening mechanism and then summing up the contributions from all the individual Eu^{3+} local environments to represent inhomogeneous broadening, the spectra will be simulated in detail, and they will be quantitatively compared with experimental optical spectra. In Sec. IV, we will investigate various factors that characterize the local environment and that may influence the energy levels of the Eu^{3+} ions. In particular, the influence of the crystal-field strength S on the energy levels will be analyzed. In Sec. V, the relation between the crystal-field strength components S_k and the local environment of Eu^{3+} ions will be analyzed in terms of the distributions of the ligand angular positions and ligand distances. In Sec. VI, we discuss the significance of these results for understanding which local environments reduce inhomogeneous broadening. Finally in Sec. VII, we conclude.

II. MOLECULAR DYNAMICS SIMULATIONS

A. Molecular dynamics method

Molecular dynamics has been widely applied to investigate glass structures.[4,13–15] In this paper molecular dynamics is carried out using the DLPOLY program.[16] A very similar procedure has previously been used by the authors to study europium-doped silicate glass where potential parameters for Eu^{3+} ion were presented.[15]

The form of the interatomic potential used was specifically developed for modelling silicate glasses:[17]

$$U_{ij}(r) = \frac{z_i z_j e^2}{r} + D_{ij}\{[1 - e^{-a_{ij}(r-r_{ij})}]^2 - 1\} + \frac{C_{ij}}{r^{12}}. \quad (1)$$

The three terms in Eq. (1) correspond to the long-range Coulomb potential, short-range Morse potential, and the repulsive potential, respectively. The values of potential parameters in Eq. (1) are listed in Table I.

For the Coulomb potential, partial ionic charges are used: $+1.8e$ for Eu, $-1.2e$ for O, $+0.6e$ for Na, and $+2.4e$ for Si. The Coulomb interactions are evaluated by the Ewald method,[18] using a cut-off radius of 12.0 Å and an Ewald precision factor of 10^{-5}. The short-range interaction cutoff is 7.6 Å. The integration of Newton's equations uses the Verlet Leapfrog algorithm[19] with a time step of 2 fs.

The number of atoms in the simulation box is a very important factor, particularly when looking for dopant-related structural information with high statistical quality. Models of europium-doped sodium disilicate glasses have been made with two compositions representing 0.2mol% and 1.0 mol% Eu_2O_3 doping shown in Table II. The box size was chosen to represent the experimental density of sodium disilicate glass.

Each molecular dynamics simulation consists of six stages. In the first three stages, the system equilibrates at the temperatures 6000 K, 3500 K, and 2200 K for 80 000 time steps. In the fourth stage, the system continuously quenches from 2200 K to 300 K with a quenching rate of 10^{13} K/s. This quenching process leads to the formation of a glass.[15]

TABLE I. Interatomic potential parameters.[15]

Pair (ij)	D_{ij}(eV)	a_{ij}(Å^2)	r_{ij}(Å)	C_{ij}(eV Å)
O-O	0.042395	1.379316	3.618701	22.0
Si-O	0.340554	2.006700	2.100000	1.0
Na-O	0.023363	1.763867	3.006315	5.0
Eu-O	0.000139	2.013200	4.351360	3.0

TABLE II. Structure parameters of the models.

	0.2mol%	1mol%
$Eu_2O_3 : Na_2O : SiO_2$	0.2 : 33.8 : 66	1 : 33 : 66
Number of Eu^{3+} ions	20	100
Number of Na^{+} ions	3380	3300
Number of Si^{4+} ions	3300	3300
Number of O^{2-} ions	8320	8400
Total number of atoms	15020	15100

In the fifth stage, the system equilibrates at room temperature for 80 000 time steps. Finally, structural data were collected in the sixth stage every 50 time steps, with a total of 1600 configurations.

B. Glass models

The models of glass structures in Fig. 2 show that the Eu^{3+} ions are well separated inside the glasses. It is not the purpose of this paper to present detailed structural analysis other than the local environments of Eu^{3+} ions. However, some standard structural quantities are presented to show that these are realistic models. The radial distribution function and the bond angle distribution functions are calculated from the 1600 configurations and are shown in Fig. 3 and Fig. 4, respectively.

The radial distribution function $T_{ij}(r)$ is defined as[13]

$$T_{ij}(r) = \frac{1}{r}\left\{\frac{1}{N_i}\sum_{l=1}^{N_i}\left[\sum_{m=1}^{N_j}\delta(r - R_{lm})\right]\right\}, \qquad (2)$$

where N_i is the number of atoms of type i. The coordination number CN is obtained from the integration of $rT_{ij}(r)$ and gives the average number of atom type j as a function of distance r from atom type i. The peaks in $T_{ij}(r)$ give information about local structure in the glass. The first peak at 1.6 Å corresponds to silicon coordinated by 4.0 oxygens. The next peaks are Na-O at 2.3 Å with average CN of 5.0 and Eu-O at 2.3 Å with average CN of 5.7. Figure 3 also shows that the 0.2mol% and 1mol% models have very similar $T_{ij}(r)$ except for the Eu-Eu distribution. For the 0.2mol%, the Eu^{3+} ions are well isolated with no Eu-Eu distance less than 5 Å, whereas there are a few Eu^{3+} ions separated by 3–5 Å for the 1mol% sample.

Figure 4 shows that the bond angle distribution functions of the two models are very similar. The peaks at 109° and 142° correspond to SiO_4 tetrahedra and Si-O-Si bonds in the silica network. The large range of bond angles for O-Eu-O implies that Eu^{3+} do not have well-defined coordination polyhedron and lack site symmetry as expected in a glass. Nevertheless, there are broad peaks near 90° and 180° that roughly resemble a CN of 6 (e.g., approximate octahedral geometry).

The models of Eu_2O_3-doped sodium disilicate glass can be compared with experimental diffraction measurements of sodium disilicate glass. A diffraction experiment measures the

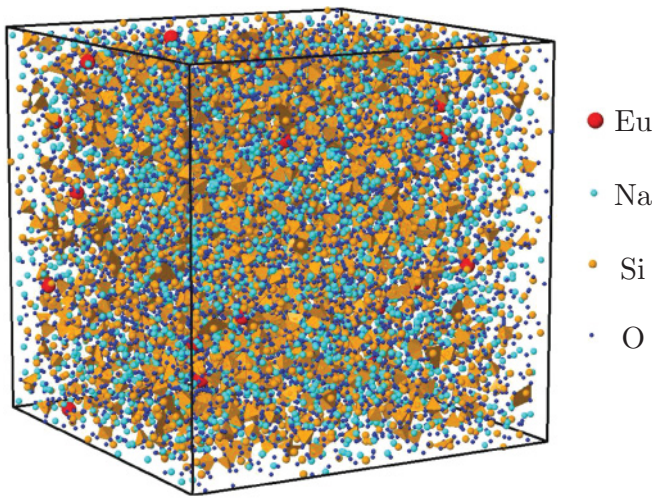

(a) 0.2mol%

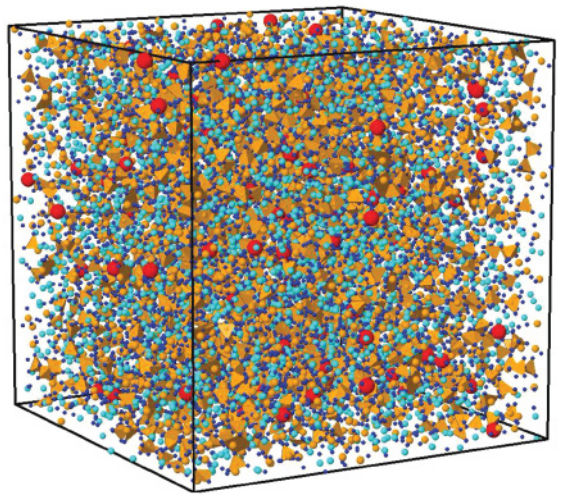

(b) 1mol%

FIG. 2. (Color online) Models of Eu_2O_3-doped sodium disilicate glass generated by molecular dynamics. Eu ions are large red spheres, Na ions are medium cyan spheres, the silicate network is yellow, and O ions are small blue spheres.

intensity of scattering as represented by the structure factor $S(Q)$ as a function of scattering angle 2θ with Q being the scattering wave vector:

$$Q = 4\pi \sin(\theta)/\lambda, \qquad (3)$$

where λ is the wavelength of the x ray or neutron. The structure factor $S(Q)$ has a precise dependence on the $T_{ij}(r)$ of the glass structure as shown by the following equation:[20]

$$Q[S(Q) - 1] = \int \sum_{ij} w_{ij}(Q)[T_{ij}(r) - 4\pi r\rho_j]\sin(Qr)dr, \qquad (4)$$

where $w_{ij}(Q)$ are the weighting factors for scattering of x rays or neutrons by atom types i and j and ρ_i is the atomic number density of atom type j.

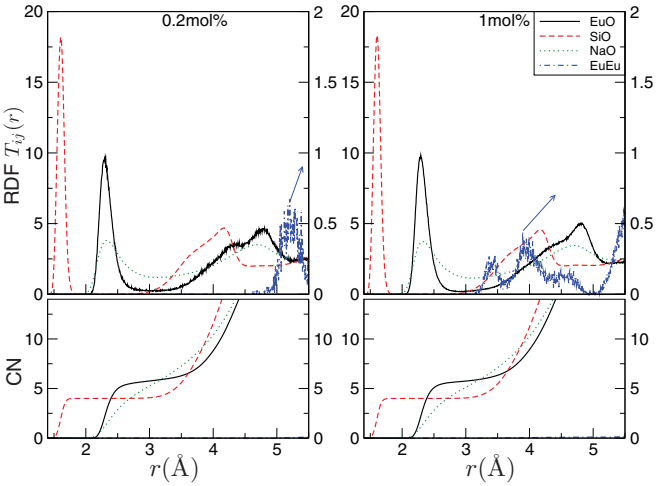

FIG. 3. (Color online) Radial distribution functions $T_{ij}(r)$ and the coordination number (CN).

Figure 5 shows the calculated $S(Q) - 1$ for the 1 mol% sample compared with the experimental x-ray and neutron[21] diffraction. As no diffraction data were available for Eu_2O_3-doped sodium disilicate glass, the comparison has been made with undoped sodium disilicate glass. The neutron diffraction data are from the literature[21] and the x-ray diffraction data were previously collected by the authors at Station 9.1 of the SRS (Daresbury Laboratory, UK).[22] It can be assumed that there is negligible contribution to the diffraction pattern from Eu^{3+} ions because of the very low concentration of Eu^{3+} ions in the glass. In fact, the agreement between $S(Q)$ for model and experiment is very good.

III. ABSORPTION AND EMISSION SPECTRA CALCULATIONS

The glass structures generated from molecular dynamics will be used to calculate the Eu^{3+} ion emission and absorption spectra. For calculating the energy levels of an individual Eu^{3+} ion, the total Hamiltonian consists of three contributions:

$$H_{\text{total}} = H_{\text{ion}} + H_{\text{correct}} + H_{\text{CF}}. \tag{5}$$

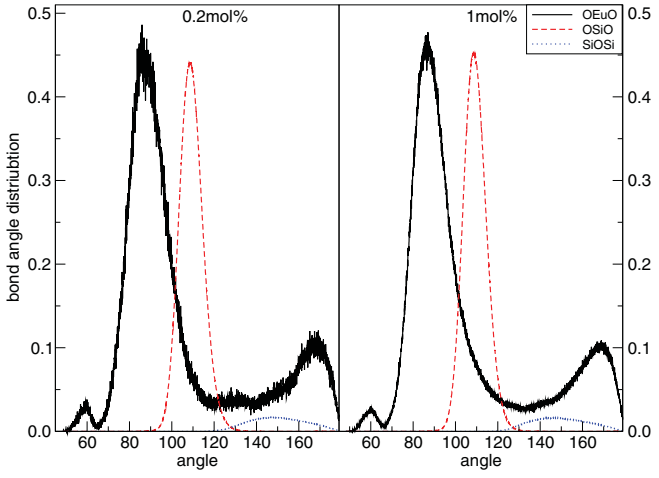

FIG. 4. (Color online) Bond angle distribution function.

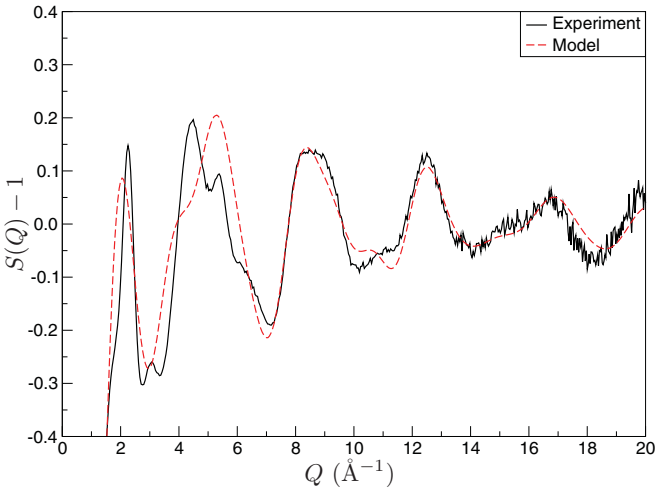

(a) X-ray diffraction

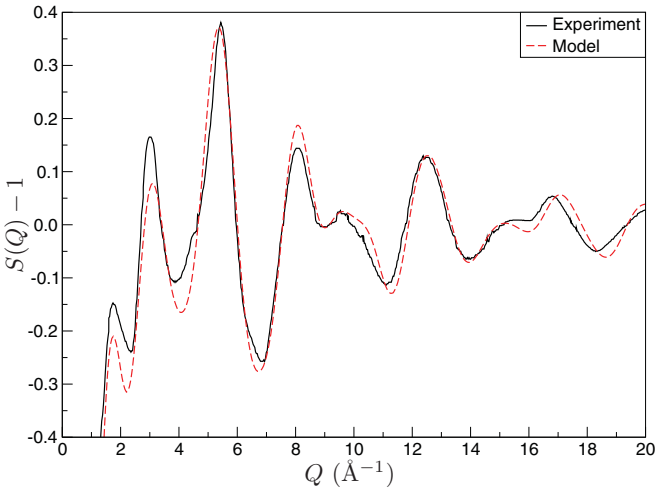

(b) neutron diffraction

FIG. 5. (Color online) Comparison of the 1 mol% model with experimental diffraction data for sodium disilicate glass.

A. Free ion model

The most important part of the free ion Hamiltonian is[23]

$$H_{\text{ion}} = H_0 + \sum_{k=2,4,6} F^{(k)} f_k + \zeta A_{\text{so}}, \tag{6}$$

where H_0 includes the kinetic energy and the electron-nucleus interaction. H_0 will not be considered, since it results in identical $4f$ energy levels and hence does not contribute to the $4f$ energy levels splitting. f_k and A_{so} represent the angular parts of the electron-electron and spin-orbital interactions, respectively. $F^{(k)}$ are electron-electron repulsion integrals that are related to the radial dependence of $4f$ electron wave function. ζ is the spin-orbital coupling parameter. H_{correct} in Eq. (5) includes additional terms that affect the $4f$ energy levels.[9,23]

The parameter values in Eq. (6) for Eu^{3+} ions are listed in Table III.

TABLE III. Parameter values within H_{ion} for free Eu^{3+} ions (unit cm^{-1}).[23]

$F^{(2)}$	$F^{(4)}$	$F^{(6)}$	ζ	α	β	γ
83125	59268	42560	1338	20.16	−566	1500

B. Crystal-field theory

The crystal field describes the perturbations to $4f$ electron wave functions that result from the surroundings and that are not experienced by a free ion. Historically, the crystal field is considered from the starting point of an electrostatic model. The crystal-field Hamiltonian H_{CF} can be written as the sum of the Coulomb interactions between the $4f$ electrons and the surrounding charge distribution:

$$H_{\text{CF}} = -\frac{e}{4\pi\varepsilon_0}\sum_{i=1}^{n} V(\mathbf{r}_i), \tag{7}$$

where n is the number of f electrons, i.e., $n = 6$, for a Eu^{3+} ion. Here $-e$ is the electron charge, ε_0 is the vacuum permittivity, and $\mathbf{r}_i$ is the position of the electron. The crystal-field potential describes the surrounding charge distribution including a $1/r$ term (relative to the $4f$ electron). Following the point-charge electrostatic model (PCEM),[5] we have

$$V(\mathbf{r}_i) = \sum_{j=1}^{L}\sum_{k=0}^{\infty}\sum_{q=-k}^{k}\frac{q_j e r_i^k}{R_j^{k+1}} C_q^{(k)*}(j) C_q^{(k)}(i), \tag{8}$$

where $\mathbf{R}_j$ is the ligand ion position and q_j is the ligand ion charge (for example, $q_j = -2$ for O^{2-}). $C_q^{(k)}(i)$ and $C_q^{(k)}(j)$ are the renormalized spherical tensor operators for the electrons and ligands.[6]

The interior spherical multipole moments of the charge distribution are[24]

$$I_q^k = \sum_{j=1}^{L}\frac{q_j e}{R_j^{k+1}} C_q^{(k)*}(j). \tag{9}$$

It then can be seen that the widely used Stevens crystal-field parameters A_q^k can be written in terms of the multipole moments:[25]

$$A_q^k = -\frac{e}{4\pi\varepsilon_0} I_q^k. \tag{10}$$

It can be seen that the Stevens crystal-field parameters differ from the multipole moments only by a constant prefactor. Since the electron position r_i is a quantum mechanical quantity, r_i^k will be replaced by the expected value $\langle r_i^k\rangle$. Finally, the crystal-field Hamiltonian can then be written

$$H_{\text{CF}} = \sum_{i=1}^{n}\sum_{k=0}^{\infty}\sum_{q=-k}^{k}\langle r_i^k\rangle A_q^k C_q^{(k)}(i). \tag{11}$$

An alternative representation of the crystal-field parameters was introduced by Wybourne:[26]

$$\begin{aligned} B_q^k &= \langle r_i^k\rangle A_q^k \\ &= -\frac{e^2}{4\pi\varepsilon_0}\sum_{j=1}^{L}\langle r_i^k\rangle\frac{q_j}{R^{k+1}} C_q^{(k)*}(j). \end{aligned} \tag{12}$$

TABLE IV. Parameter values in Eq. (14) and Eq. (21). The unit of $\overline{B}_k$ is cm^{-1} and $\overline{A}_k^{(\lambda)}$ is 10^{-12} cm^{-1}.

$\overline{B}_2$	$\overline{B}_4$	$\overline{B}_6$	τ_2	τ_4	τ_6
725	441	378	4	6	7
$\overline{A}_1^{(2)}$	$\overline{A}_3^{(2)}$	$\overline{A}_3^{(4)}$	$\overline{A}_5^{(4)}$	$\overline{A}_5^{(6)}$	$\overline{A}_7^{(6)}$
−440	−410	50	220	−40	−250
$\tau_1^{(2)}$	$\tau_3^{(2)}$	$\tau_3^{(4)}$	$\tau_5^{(4)}$	$\tau_5^{(6)}$	$\tau_7^{(6)}$
3	5	5	7	7	9

Equation (12) is the expression for B_q^k within the PCEM.

It has been proved that for rare-earth ions, only $k = 2,4,6$ are needed to account for the splitting of $4f$ electron energy levels.[6,26] For Eu^{3+} ion this gives

$$H_{\text{CF}} = \sum_{i=1}^{6}\sum_{k=2,4,6}\sum_{q=-k}^{k} B_q^k C_q^{(k)}(i). \tag{13}$$

C. Superposition model

As discussed in the introduction, the PCEM is oversimplified because the interactions between the electrons and ligand ions are more complicated than a pure electrostatic interaction.[6] However, the superposition principle from the PCEM is that the Hamiltonian is a sum over interactions with individual ligands, and this remains valid for a realistic model of the crystal field, in which overlap and covalency contribute significantly to the crystal field. By taking account of all the overlap, covalent, and other interactions, the superposition model (SM) has been found to be more realistic and accurate.[6] Via the superposition model, B_q^k is expressed as[6]

$$B_q^k = \sum_{j=1}^{L}\overline{B}_k\left(\frac{R_0}{R_j}\right)^{\tau_k} C_q^{(k)*}(j), \tag{14}$$

where $\overline{B}_k$, τ_k, and R_0 are empirical parameters. R_0 is taken as 2.24 Å.[6] Note that the complex interactions between the $4f$ electrons and a ligand are described by the intrinsic parameter $\overline{B}_k$ where the dependence of these interactions on ligand distance is given by the factor $(\frac{R_0}{R_j})^{\tau_k}$. The published fitted parameters for Eu^{3+} ions with oxygen ligands are listed in Table IV.

The superposition model is a method for calculating the crystal-field parameters that normally takes into account only the nearest neighboring ligand ions because these dominate the covalent and overlap interactions.[6] For the current simulation, the cut-off radius is taken as 3 Å to obtain the nearest-neighbor oxygens of each Eu^{3+} ion.

After setting up all the Hamiltonians in Eq. (5), the coupled basis $|\alpha LSJM_J\rangle$ is chosen for the current calculation, where α is the seniority number.[9] For the Eu^{3+} ion calculations, the chosen basis starts from $^7F_0$ and goes to $^5L_6$; consequently, the Hamiltonian is a 78×78 matrix. It is noted that an uncoupled basis can also be employed.[27] The matrix elements to calculate

the energy levels are

$$\langle \alpha' L' S' J' M'_J | H_{\text{total}} | \alpha L S J M_J \rangle. \tag{15}$$

The energy levels and associated eigenstates $|\psi_a\rangle$ can be computed by diagonalizing this matrix.[28] The resulting eigenstates of all six $4f$ electrons together will be a mixing of the basis states and can be expressed as

$$|\psi_a\rangle = \sum_v c_v |\alpha L S J M_J\rangle_v, \tag{16}$$

where c_v are the coefficients of the basis states.

During the calculations, full $|\alpha L S J M_J\rangle$ has been used and the free-ion parameters in Table III are assumed to be fixed. Of course, when the lanthanide ions are doped into crystals, the covalency and nephelauxetic effect will change the values of the free-ion parameters but their variations will be relatively small because all lanthanide ions in this system are affected by the same type of ligands.

D. Transition probability

Denoting $|\psi_a\rangle$ as the initial state and $|\psi_b\rangle$ as the final state for an optical transition, the corresponding line strength for the electric dipole (ED) transition is

$$S^{\text{ED}}_{a,b,\varepsilon} = e^2 |\langle \psi_a | D_\varepsilon | \psi_b \rangle|^2, \tag{17}$$

where D_ε is the effective vector operator. Here $\varepsilon = 0, \pm 1$ represents the spherical polarization bases. With the assumption of cylindrical symmetry for each ligand, D_ε can be calculated by means of the Reid-Richardson parametrization:[6,9,29,30]

$$D_\varepsilon = \sum_{\lambda=2,4,6} \sum_{k=\lambda\pm1} \sum_{q=-k}^{k} A_q^{(\lambda,k)} \times U^{(\lambda)}_{(q+\varepsilon)} (-1)^\varepsilon \langle \lambda(q+\varepsilon), 1-\varepsilon | k, q \rangle \tag{18}$$

where $U^{(\lambda)}_{(q+\varepsilon)}$ is the unit tensor operator and $\langle \lambda(q+\varepsilon), 1-\varepsilon | k, q \rangle$ is the Clebsch-Gordan coefficient (note that the indices we label as k, q are often found in the literature labeled as t, p).[8]

$A_q^{(\lambda,k)}$ are called the transition probability parameters. They are related to A_q^k in Eq. (11) and $\Xi(k,\lambda)$ in Axe's paper[31] based on the Judd-Ofelt theory:[6,32,33]

$$A_q^{(\lambda,k)} = -A_q^k \, \Xi(k,\lambda) \frac{(2\lambda+1)}{(2k+1)^{1/2}}. \tag{19}$$

Therefore, the well-known Judd-Ofelt parameters $\Omega^{(\lambda)}$ can be expressed as:[10,30]

$$\Omega^{(\lambda)} = \frac{1}{2\lambda+1} \sum_{k=\lambda\pm1} \sum_{q=-k}^{k} \left| A_q^{(\lambda,k)} \right|^2. \tag{20}$$

$A_q^{(\lambda,k)}$ represent the influence of the local environment due to the ligands. Therefore, similar to the calculation of B_q^k in Eq. (14), a superposition model can be applied to calculate $A_q^{(\lambda,k)}$ using:[9,10]

$$A_q^{(\lambda,k)} = \sum_j^L \overline{A}_k^{(\lambda)} \left(\frac{R_0}{R_j} \right)^{\tau_k^{(\lambda)}} C_q^{(k)*}(j). \tag{21}$$

The values of $\overline{A}_k^{(\lambda)}$ and $\tau_k^{(\lambda)}$ are listed in Table IV. As before, $\overline{A}_k^{(\lambda)}$ are the intrinsic parameters representing interaction of $4f$ electrons with ligands and the dependence of the interactions on ligand instance is given by the factor $(\frac{R_0}{R_j})^{\tau_k^{(\lambda)}}$. There is little literature on $\overline{A}_k^{(\lambda)}$ values for Eu^{3+} in silicates, so the values in Table IV have been chosen to obtain calculated transition intensities that are in reasonable agreement with experiment. Nevertheless the values of $\overline{A}_k^{(\lambda)}$ in Table IV are similar to those which have been reported for Eu^{3+} in fluoride and tungstate crystals.[10]

The line strength for the magnetic dipole (MD) transition is

$$S^{\text{MD}}_{a,b} = (\mu_B/e)^2 [\langle \psi_a | \mathbf{L} + 2\mathbf{S} | \psi_b \rangle]^2, \tag{22}$$

where μ_B is the Bohr magneton. $\mathbf{L}$ and $\mathbf{S}$ are the total orbital and spin angular momentum, respectively. Combining the ED and MD transitions, the oscillator strength is[34]

$$f_{ab} = \frac{8\pi^2 m c E_{ab}}{3he^2} \left[\chi S^{\text{ED}}_{ab} + \chi' S^{\text{MD}}_{ab} \right], \tag{23}$$

where m is the electron mass, h is the Plank constant, c is the speed of light. E_{ab} is the energy difference between $|\psi_a\rangle$ and $|\psi_b\rangle$. Here χ and χ' are the Lorentz correction factors for the ED and MD transitions, respectively.[35] For emission,

$$\begin{cases} \chi = \frac{\eta(\eta^2+2)^2}{9} \\ \chi' = \eta^3 \end{cases}, \tag{24}$$

and for absorption,

$$\begin{cases} \chi = \frac{(\eta^2+2)^2}{9\eta} \\ \chi' = \eta \end{cases}, \tag{25}$$

where η is the refractive index and is taken as 1.505 for sodium disilicate glass.[35]

The Lorentzian profile arising from the energy-time uncertainty principle is employed for the homogeneous lineshape broadening:[11,36]

$$g(E) = \frac{W}{2\pi} \frac{1}{(E - E_{ab})^2 + (W/2)^2}, \tag{26}$$

where W is the full width at half maximum (FWHM), which is taken to be 10 cm^{-1}.[37,38] This broadening is normally approximated as being the same for each Eu^{3+} ion. The inhomogeneous broadening is due to the different local environments of Eu^{3+} ions and is calculated by summing up the contributions from all the Eu^{3+} ions. In previous calculations of luminescence spectra for glasses,[4] after summing up the contributions from all the Eu^{3+} ions, the inhomogeneous broadening was augmented by using a Gaussian function with large FWHM of 75 cm^{-1}. The current work is the first where the inhomogeneous broadening is entirely due to the sampling over different rare-earth local environments in the model.

In summary, the whole methodology can be described using the flowchart in Fig. 6.

For the absorption starting from $^7F_1$ level, the Boltzmann distribution can be taken into account. According to the Boltzmann distribution, the ratio of $^7F_1$ to $^7F_0$ in contributing to the absorption spectrum would be about 0.15 at room temperature, whereas the ratio of $^7F_2$ to $^7F_0$ is about 0.01.

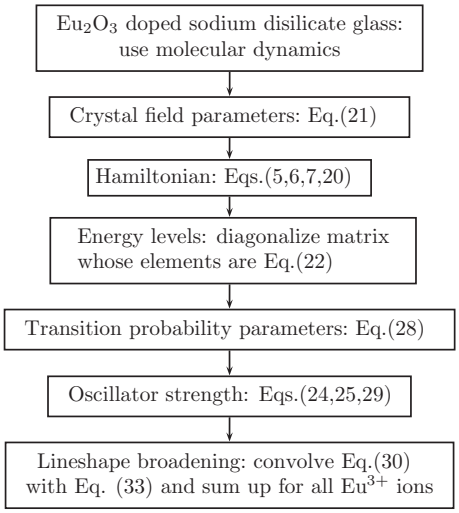

FIG. 6. (Color online) Flowchart for calculation of optical spectra.

Therefore $^7F_2$ does not need to be considered for the absorption spectrum.

E. Simulated optical spectra

As mentioned for the molecular dynamics simulations, there are 1600 configurations during the thermal motion at room temperature. When calculating the optical spectra, this thermal motion should be taken into account. Ten snapshots during the thermal motion are used for the optical spectra generation. Following the above procedure, the simulated spectra are shown in Fig. 7 for both 0.2mol% and 1mol% models. It shows that, although the Eu^{3+} concentrations differ, their spectra are very similar. This is not surprising since the structural features of the local environments of Eu^{3+} ions are very similar in these two glass models as seen in the $T_{ij}(r)$ of Fig. 3. Experimental spectra have been published in the literature for emission in a 0.2mol% Eu_2O_3-doped sodium disilicate glass and for absorption in a 1mol% Eu_2O_3-doped sodium disilicate glass.[4] In addition, new experimental spectra have been measured by the authors in the present study on both 0.2mol% and 1mol% Eu_2O_3-doped sodium disilicate glasses (see Appendix A for details of experiment measurements). Figure 8 shows the new experimental emission spectra and that the spectra are very similar for both doping levels.

Figure 9 shows the comparison between the simulated and experimental optical spectra, including the previously reported experimental spectra,[4] and there is reasonable agreement. Figure 9(a) shows that the emission spectra from $^5D_0$ to the lower energy levels agree well with the experimental data. The quantitative absorption spectra in Fig. 9(b) also show that the transition from $^7F_0$ to the higher energy levels can be well reproduced using this methodology.

F. Radiative lifetime

The radiative lifetime τ is the reciprocal of the sum of all the emission probabilities in the emission spectrum:[39]

$$\frac{1}{\tau} = \sum_b P_{ab}, \tag{27}$$

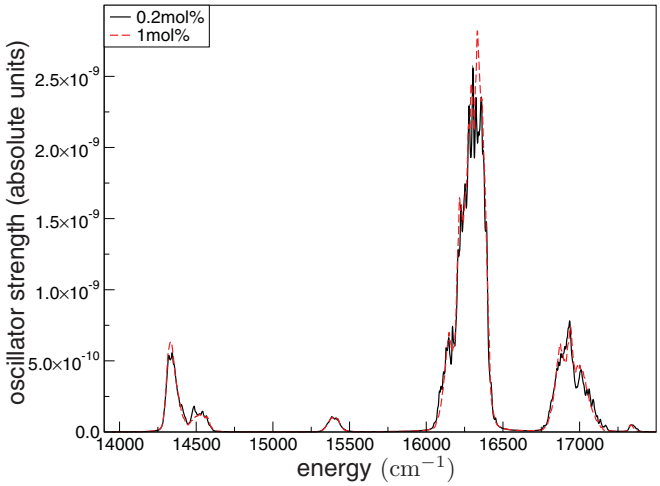

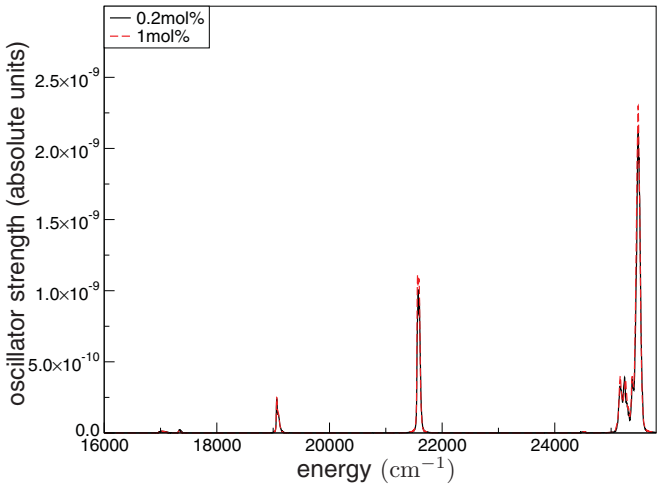

FIG. 7. (Color online) Simulated spectra for different Eu_2O_3 concentrations.

where P_{ab} is the emission probability. For Eu^{3+}, a stands for the $^5D_0$ state, and b are the lower ^7F_J levels. P_{ab} has a relation with the oscillator strength:[40]

$$P_{ab} = \frac{2\pi e^2 E_{ab}^2}{\varepsilon_0 mc} f_{ab}. \tag{28}$$

Combining with Eq. (23),

$$P_{ab} = \frac{16\pi^3 E_{ab}^3}{3h\varepsilon_0}\left[\chi S_{ab}^{\mathrm{ED}} + \chi' S_{ab}^{\mathrm{MD}}\right]. \tag{29}$$

A well-known result for the radiative lifetime is that the radiative lifetime is related to the shape of the emission spectrum:[41,42]

$$\frac{1}{\tau} = P_0 \eta^3 \left(\frac{I_{\mathrm{total}}}{I_{\mathrm{MD}}}\right), \tag{30}$$

where P_0 is the spontaneous emission probability for the $^5D_0 \rightarrow {}^7F_1$ transition in vacuum, and it is taken as $14.65\mathrm{s}^{-1}$.[41] $I_{\mathrm{total}}/I_{\mathrm{MD}}$ is the ratio of the total area of the emission spectrum to the area of the $^5D_0 \rightarrow {}^7F_1$ band. Equation (30) can be used to calculate the radiative lifetime τ from the experimental data in

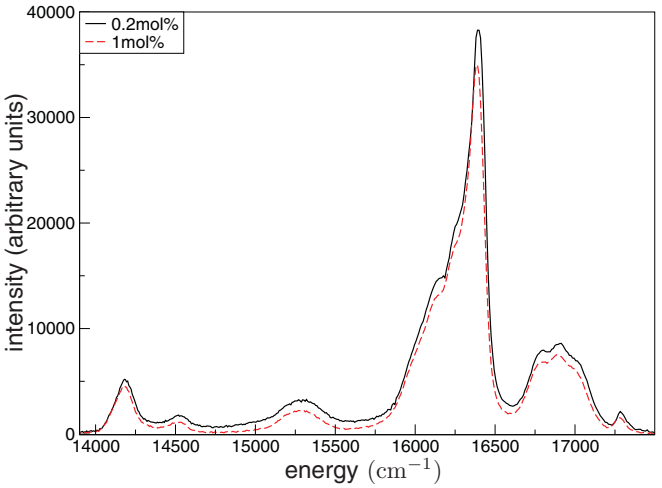

FIG. 8. (Color online) New experimental emission spectra measured by the authors for different Eu_2O_3 concentrations.

Fig. 9(a), and the value obtained is 5.2 ms. τ can be calculated using Eq. (27), and the value obtained is 6.3 ms. From Table II of Ref. 41, it can be seen that typical values of radiative life time for various Eu_2O_3-doped materials are between 3 and 10 ms. In fact, the measured lifetime from decay curves for two samples was about 3 ms. Our simulation results for lifetime are, hence, reasonably consistent with the experimental data.

IV. FACTORS INFLUENCING THE ENERGY LEVELS

A comprehensive methodology has been demonstrated to simulate the optical spectra of Eu^{3+} ions in models of Eu_2O_3-doped sodium disilicate glass. Moreover, the simulation results enable us to investigate the influence of factors from the local environment of Eu^{3+} ions on the inhomogeneous broadening. Figure 7 shows that the spectra are very similar for 0.2mol% and 1mol% models, and the 1mol% model will be chosen for the following analysis because it contains 100 Eu^{3+} ions so gives better statistics.

First, we would like to analyze the energy levels near the ground state $^7F_0$ and the first excited state $^5D_0$ with respect to the $^7F_0 \rightarrow {}^5D_0$ transition energy. In particular, the fluorescence line narrowing (FLN) technique is capable of probing Eu^{3+} ions with specific $^7F_0 \rightarrow {}^5D_0$ transition energies, and experimental FLN[43] results show that $^7F_1$ and $^7F_2$ manifolds get wider as $^7F_0 \rightarrow {}^5D_0$ transition energy increases.

Figure 10 shows the $^{2S+1}L_J$ energy levels near $^7F_0$ and $^5D_0$ that are split into manifolds with $2J+1$ separate levels when the degeneracy of M_J is removed. Figure 10 shows that as $^7F_0 \rightarrow {}^5D_0$ transition energy increases, $^7F_0$ energy level decreases in energy but the $^5D_0$ energy level remains steady. The splitting of $^7F_1$ and $^7F_2$ manifolds increases continuously with the transition energy, i.e., the splitting of manifolds increases as the $^7F_0$ energy level decreases, just as seen in the experimental FLN results.[43] These observations are also consistent with published simulation results on europium-doped fluoroaluminate glasses.[44] The splitting of $^5D_1$ and $^5D_2$ manifolds also increases as the $^7F_0 \rightarrow {}^5D_0$ transition energy increases, but the widening of ^5D_J levels is not so significant as for ^7F_J levels. Therefore, the $^7F_0$ energy level will be chosen

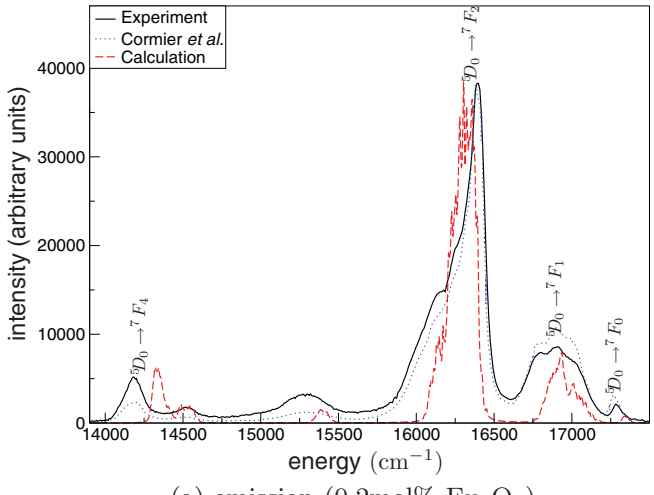

(a) emission (0.2mol% Eu_2O_3)

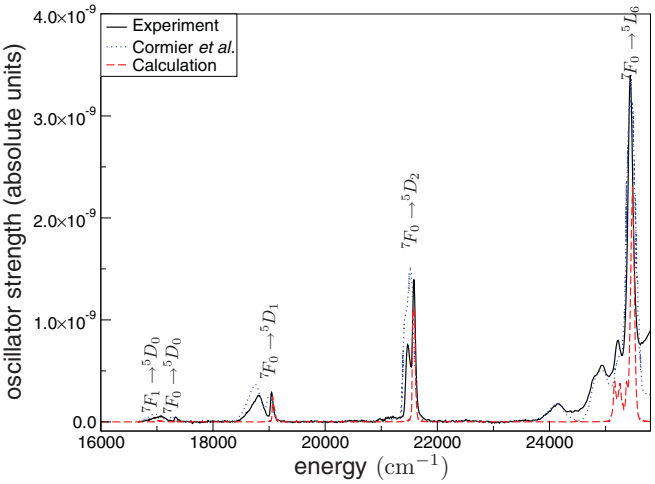

(b) absorption (1mol% Eu_2O_3)

FIG. 9. (Color online) Spectra for Eu_2O_3-doped sodium disilicate glasses. "Experiment" denotes data measured by the authors in the present study. "Cormier *et al*" denotes data measured in Ref. 4. "Calculation" denotes simulated spectra in the present study.

for the following investigations, since to a good approximation the changes in energy levels and manifolds are seen to be monotonic with the decrease in the $^7F_0$ energy level.

In order to investigate what factors from the local environment affect the $^7F_0$ level, first we would like to examine some commonly used structural quantities shown in Fig. 11. Figure 11 shows that there are no distinct correlations between the $^7F_0$ energy and the Eu^{3+} coordination number CN or distance-related quantities: the average ligand distance, $\langle R_j \rangle$; the standard deviation in ligand distance, stdevR_j; and the minimum ligand distance, minR_j.

Given that there is no obvious link between the commonly used structural quantities of Eu^{3+} ion sites and the $^7F_0$ energy level, it is necessary to look for other factors to explain the differences in energy levels from one Eu^{3+} ion site to another. In the following graphs we will maintain the distinction between the Eu^{3+} ion sites with different values of CN since CN is a fundamental descriptor of ion sites in solids.

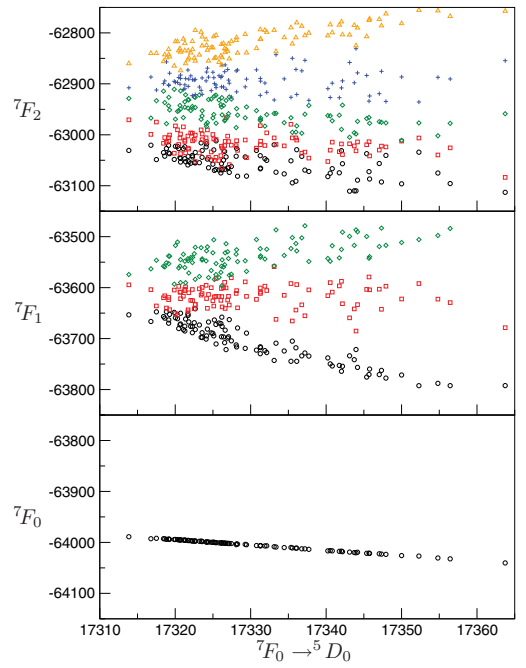

(a) ^7F_J

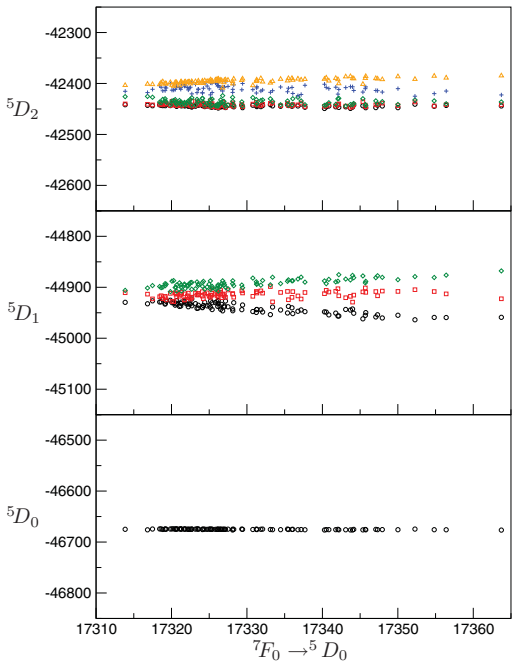

(b) ^5D_J

FIG. 10. (Color online) Energy levels versus $^7F_0 \rightarrow {}^5D_0$ transition energy (unit cm^{-1}). Different symbols are used to denote $2J+1$ levels within each $^{2S+1}L_J$ manifold.

We, first, examine the components of the ground-state wave function. Since the ground-state wave function is overwhelmingly composed of the free-ion $^7F_0$ state, it is conventional to use the label $^7F_0$ for the ground state even if the ground state is no longer composed of 100% free-ion $^7F_0$ state. The ground-state wave function also gets mixing from other free-ion states as seen from Eq. (16). Figure 12 shows the contribution of free-ion $^7F_0$ state to the ground state which is

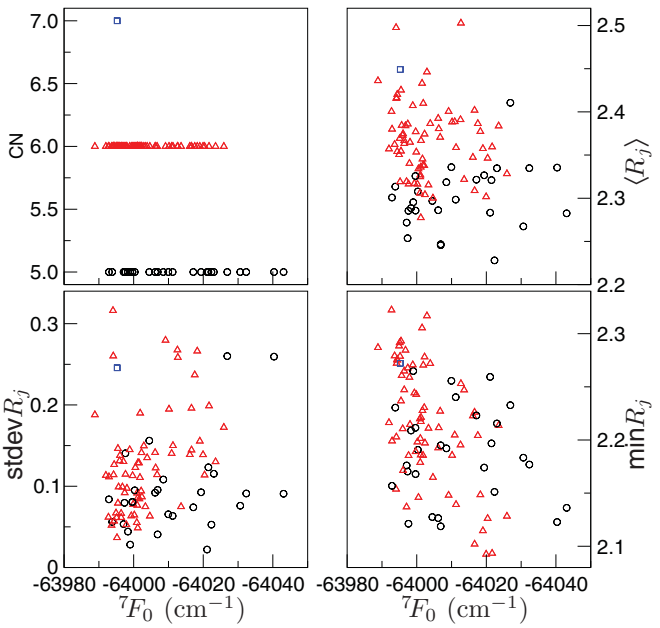

FIG. 11. (Color online) Structural quantities versus $^7F_0$ ground-state energy. (Upper left panel) Ligand coordination number CN; (upper right panel) average ligand distance $\langle R_j \rangle$ (Å); (lower left panel) standard deviation in distance (Å); (lower right panel) minimum distance (Å). Circles for CN = 5, triangles for CN = 6 and squares for CN = 7.

represented by the simulation software to two decimal places. It can be seen that the more mixing, the lower the ground-state energy.

The amount of mixing, and hence the change in the energy levels, is ultimately due to the crystal-field parameters, since the Hamiltonian in Eq. (15), which determines the ground-state energy (i.e., the lowest energy eigenvalue), is calculated from the quantities B_q^k in Eq. (13). Therefore, it is useful to look for patterns in the data that show the influence of B_q^k parameters. However, the complexity of the calculation makes it very difficult to see by algebraic inspection how the matrix

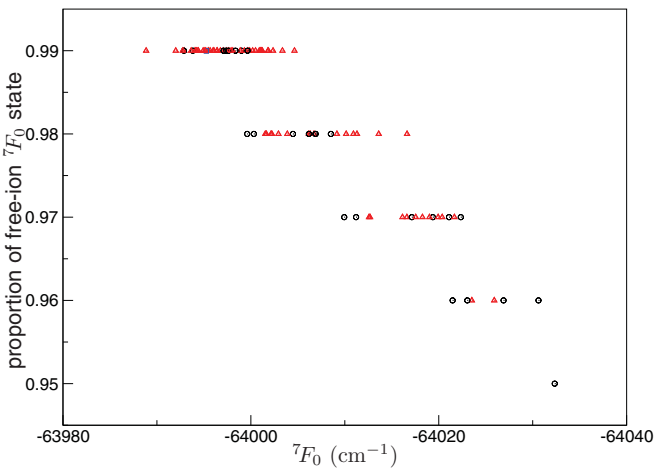

FIG. 12. (Color online) The proportion of free-ion $^7F_0$ state in the ground state versus the ground-state energy. Circles for CN = 5, triangles for CN = 6, and squares for CN = 7.

diagonalization is influenced by a particular numerical value for a B_q^k parameter with given values of k and q.

More importantly, it is known that B_q^k take significantly different values depending on the choice of axes orientations.[45] For this reason, many previous studies have assumed a certain site symmetry of C_{2v}. In a glass, any choice of coordinate axes would be arbitrary. In fact, ions with local environment in all possible orientations must be present. Therefore, it is appropriate to examine parameters that are independent of the choice of coordinate axes. For this reason the rotation-invariant crystal-field strength components S_k are often used:[46,47]

$$S_k^2 = \frac{1}{2k+1}\sum_{q=-k}^{k} |B_q^k|^2. \tag{31}$$

These second-order quantities are invariants because they depend only on angles between ligands. (It is noted that for this reason first-order rotation invariants are not possible.[6]) They offer a comparative measure of the crystal-field properties that is independent of the choice of axes orientations and, hence, can be compared across different Eu^{3+} ion sites in a glass. The crystal-field strength S_{total} is defined as

$$S_{\text{total}}^2 = \tfrac{1}{3}\left(S_2^2 + S_4^2 + S_6^2\right). \tag{32}$$

This quantity offers an indication of the overall significance of crystal-field effects.

Figure 13 shows that the crystal-field strength component S_2 increases proportionally while the $^7F_0$ ground-state energy decreases. The relations between S_4 and S_6 and the ground-state energy are more scattered. Overall the right-hand lower panel of Fig. 13 shows that a higher the crystal-field strength S_{total} tends to be associated with a lower ground-state energy due to influence from S_2. Combined with the observations in Fig. 12, it can be concluded that the stronger crystal field can lead to more mixing in the ground-state wave function that lowers the ground-state energy, and this trend is primarily due

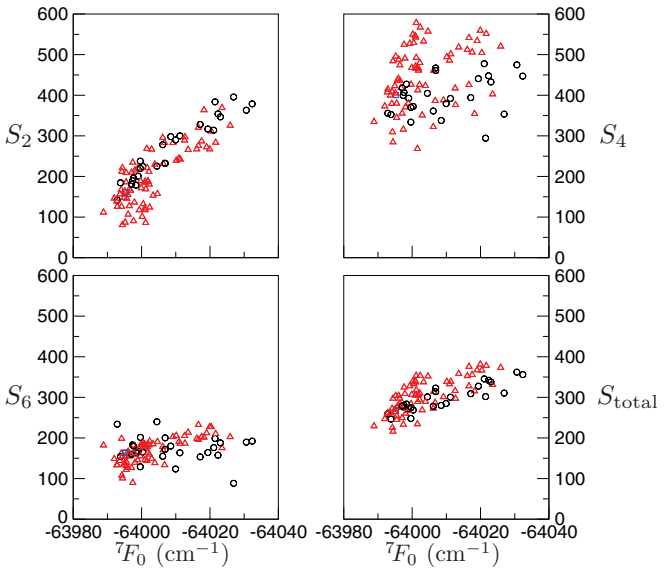

FIG. 13. (Color online) Crystal-field strength components S_k and crystal-field strength S_{total} against the $^7F_0$ ground-state energy. Circles for CN = 5, triangles for CN = 6 and squares for CN = 7.

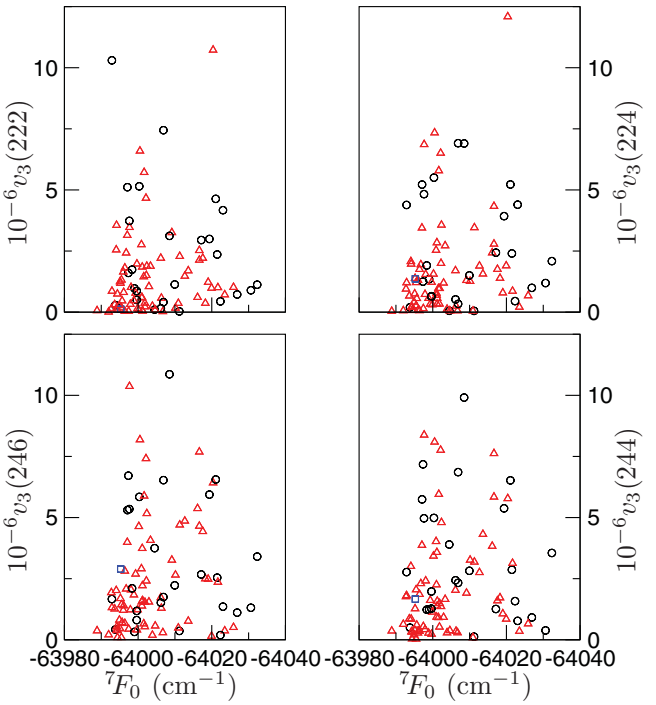

FIG. 14. (Color online) Third-order rotation invariants versus the $^7F_0$ ground-state energy. Circles for CN = 5, triangles for CN = 6, and squares for CN = 7.

to the contribution from S_2. The results in Fig. 10 show the increase of crystal-field strength and, particularly S_2, is also associated with the increase in the splitting of ^7F_J and ^5D_J manifolds. At this stage it can be noted that there is a tendency for lower S_2 values to occur for rare-earth sites with CN = 6 (triangles) than with CN = 5 (circles). This will be examined further in Sec. V.

The crystal-field strength is related to the second-order rotation invariants. Similarly, we can define third-order rotation invariants as follows:[48]

$$v_3(k_1k_2k_3) = \sum_{q_1,q_1,q_3} \begin{pmatrix} k_1 & k_2 & k_3 \\ q_1 & q_2 & q_3 \end{pmatrix} B_{q_1}^{k_1} B_{q_2}^{k_2} B_{q_3}^{k_3}, \tag{33}$$

where $(\cdots)$ in the right-hand side of Eq. (33) represents the $3j$ symbol.[48] There are nine such invariants corresponding to the nine inequivalent sets of k values: $(k_1k_2k_3) = (222)$, (224), (244), (246), (266), (444), (446), (466), (666). Some of the third-order rotation invariants are compared to the $^7F_0$ ground-state energy in Fig. 14. It shows that there is no distinguishable relation between the third-order rotation invariants and the $^7F_0$ ground-state energy. This is perhaps not surprising since the local environment of Eu^{3+} ions does not have any symmetry and the third-order invariations depend on angles between three ligands that are probably not strongly correlated.

V. RELATION BETWEEN THE CRYSTAL-FIELD STRENGTH COMPONENTS AND THE LOCAL ENVIRONMENT

As was shown in Sec. IV, the crystal-field strength S_{tot} as well as its components S_k play a key role in influencing the $^7F_0$

ground-state energy and also the splitting of ^7F_J manifolds. In this section, we want to examine the contributions to S_k and how these are related to ligand positions $\mathbf{R}_j = (R_j,\theta_j,\phi_j)$. In fact, Eq. (31) shows that S_k depends on B_q^k, and Eq. (14) shows that B_q^k depends on ligand distance via quantity $(\frac{R_0}{R_j})^{\tau_k}$ and on ligand angular position via quantity $C_q^{(k)}(j)$.

It is known that for two independent variables x and y,

$$\left(\frac{1}{L}\sum_{j=1}^{L} x_j\right)\left(\frac{1}{L}\sum_{j=1}^{L} y_j\right) = \frac{1}{L}\left(\sum_{j=1}^{L} x_j y_j\right). \tag{34}$$

If $C_q^{(k)}(j)$ and $(\frac{R_0}{R_j})^{\tau_k}$ are assumed to be independent for any given ligand j, following Eq. (34) we can rewrite Eq. (14) as

$$\begin{aligned} B_q^k &= \sum_{j=1}^{L}\left[\overline{B}_k\left(\frac{R_0}{R_j}\right)^{\tau_k} C_q^{(k)*}(j)\right] \\ &\approx \left[\frac{1}{L}\sum_{j=1}^{L} C_q^{(k)*}(j)\right] \times \left[\sum_{j=1}^{L}\overline{B}_k\left(\frac{R_0}{R_j}\right)^{\tau_k}\right] \\ &= Q_q^{(k)} \times T_k, \end{aligned} \tag{35}$$

where $\overline{B}_k$ is a constant and the effects of angular positions and distances of ligands can be described separately using the functions:

$$Q_q^{(k)} = \frac{1}{L}\sum_{j=1}^{L} C_q^{(k)*}(j) \tag{36}$$

and

$$T_k = \sum_{j=1}^{L}\overline{B}_k\left(\frac{R_0}{R_j}\right)^{\tau_k}, \tag{37}$$

where the latter does not depend on q. In fact $Q_q^{(k)}$ are the bond-orientational order parameters previously defined in the literature.[49] The assumption that $C_q^{(k)}(j)$ and $(\frac{R_0}{R_j})^{\tau_k}$ are independent means that ligand angular positions (θ_j,ϕ_j) are not influenced by ligand distances R_j and vice versa.

We can then approximate S_k using

$$\begin{aligned} S_k'^2 &= \frac{1}{2k+1}\sum_{q=-k}^{k}\left|B_q^k\right|^2 \\ &\approx \frac{1}{2k+1}\sum_{q=-k}^{k}\left|Q_q^{(k)}\right|^2 T_k^2 \\ &= Q_k^2 T_k^2. \end{aligned} \tag{38}$$

In this case S_k' are proportional to Q_k, where Q_k are the rotation invariants of the bond-orientational order and are defined as[49]

$$Q_k^2 = \frac{1}{2k+1}\sum_{q=-k}^{k}\left|Q_q^{(k)}\right|^2. \tag{39}$$

The bond-orientational order parameters $Q_q^{(k)}$ have values that depend on the choice of axes but, as discussed in Sec. IV, a rotationally invariant quantity is needed for describing local environments in glasses. In fact, previous studies[49,50] have used Q_k^2 to characterize the angular correlations present in local environments of atoms in disordered materials.

To consider the effects of ligand angular position and distance independently, we approximate the crystal-field strength components using Eq. (38) as

$$S_k' = Q_k T_k, \tag{40}$$

and, by analogy with Eq. (32), we define an approximation for the crystal-field strength

$$S_{\text{total}}'^2 = \tfrac{1}{3}\left(S_2'^2 + S_4'^2 + S_6'^2\right). \tag{41}$$

The assumption that ligand angular position and ligand distance are independent leads to the prediction that $S_k' = Q_k \times T_k$ from Eq. (40) will be equal to S_k from Eq. (31). Figure 15 shows this is a very good approximation for $S_4' = S_4$ and $S_6' = S_6$ and hence a fair approximation for $S_{\text{total}}' = S_{\text{total}}$. The values of S_2' are roughly equal to S_2, but S_2' tends to underestimate S_2, so the approximation of independence is less accurate in this case.

Figure 16 enables a separate study of the roles of ligand angular position, as represented by the rotational invariants of bond-orientational order Q_k in Eq. (36), and ligand distance, as represented by T_k in Eq. (37), in contributing to the crystal-field strength components S_k (and hence S_{total}). Assuming independent effects from ligand angular position and ligand distance, Fig. 16 can be used to see which factor, i.e., Q_k or T_k, is more important for explaining the variation in S_k from one Eu^{3+} ion site to another. It is seen that the large variations in the values of S_k corresponds with large variations in the values of Q_k. Instead, the values of T_k change by a small proportion. S_6 does not show any strong correlations with Q_6 or T_6 although S_6 is correlated with $Q_6 \times T_6$ as shown in Fig. 15. Instead, S_4 is approximately proportional to Q_4 that varies significantly, while S_4 is only slightly correlated with T_4 which varies less. For Q_2 and T_2, the assumption of independence is of limited

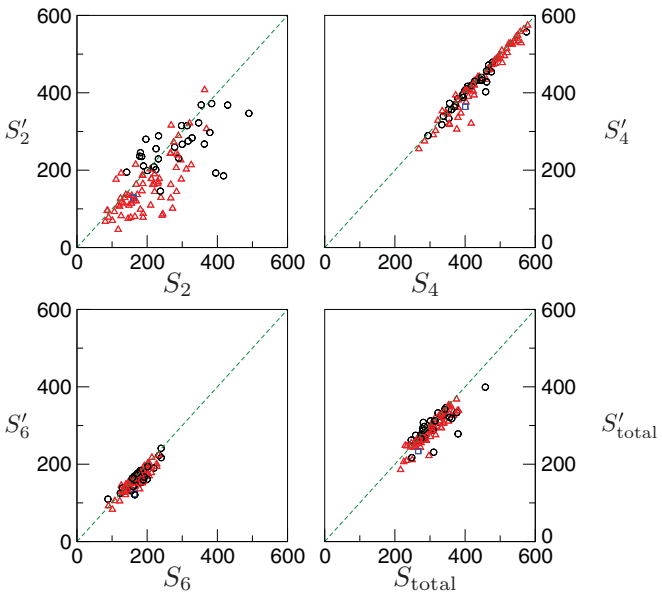

FIG. 15. (Color online) Approximations to the crystal-field strength as well as its components. Circles for CN = 5, triangles for CN = 6, and squares for CN = 7.

accuracy, but the rough trends are that S_2 is proportional to Q_2, while S_2 is not proportional to T_2 that is independent of S_2. This suggests that most variation in S_k from one Eu^{3+} site to another is due to the variation in Q_k.

VI. DISCUSSION

The results presented here provide a basis for further understanding the role of local environment for influencing luminescence properties of rare-earth ions in oxide glasses. Before continuing discussion of this point, we make some further comments on the methodology.

The superposition model (SM) plays a key role in our methodology. This approach was taken as a deliberate choice to avoid the point charge electrostatic model (PCEM). The PCEM has been extremely influential in the development of crystal-field theory and has been used in previous calculations of crystal-field effects in glasses. Nevertheless, the PCEM has been criticized because it ignores short-range covalent and overlap interactions.[6]

It is perhaps surprising that the PCEM is still a conceptually useful way to introduce crystal-field theory. The crystal-field Hamiltonian $H_{\rm CF}$ is a function of the vectors $\mathbf{r}_i$ and $\mathbf{R}_j$ and such a function may be expressed as an expansion of spherical harmonics $C_q^{(k)}(i)$ and $C_q^{(k)*}(j)$ and powers of r_i and R_j. For the PCEM the function goes as the inverse ligand distance and the expansion involves factors of r_i^k and $R_j^{-(k+1)}$ (for $r_i < R_j$). In general for a function that goes as the inverse nth power of distance the expansion involves factors r_i^k and $R_j^{-(k+n)}$.[51] Interestingly the superposition model coefficients τ_k used to calculate B_q^k and coefficients $\tau_k^{(\lambda)}$ used to calculate $A_k^{(\lambda,q)}$ are equal to $k+2$ (there is a single exception that is $\tau_6 = 7$) which suggests $n = 2$.

The role of molecular dynamics in our methodology is well established, as this is a standard and frequently used technique for studying glass structures, including in previous simulations of optical spectra. This is notwithstanding the acknowledged limitation of molecular dynamics simulations of glasses, which is the unrealistic quench rate.[13] It is noteworthy that the simulated optical spectra are extremely similar for models with different doping levels of 0.2mol% and 1.0mol% Eu_2O_3. This was also seen in experiment and implies that Eu^{3+} ions at these concentrations are well mixed in the glass matrix and not significantly affected by Eu-Eu interactions, both in the models and in experimental glasses.

The role of symmetry also deserves emphasis. The values of the crystal-field parameters B_q^k differ for different choices of axes orientations and, hence, would differ if the same model of glass structure was rotated by 90°. However, this has no effect on the calculation of observable quantities such as optical spectra that must be independent of the choice of axes orientation. In general, any given Eu^{3+} ion site will have 27 unique B_q^k parameters, and these produce the splitting of ^7F_J manifolds, e.g., three levels for $^7F_1$. The degeneracy makes it impossible to uniquely extract B_q^k parameters from an experimental fluorescence line narrowing (FLN) spectra. For this reason previous experimental FLN studies[43] have assumed rare-earth sites have C_{2v} symmetry, since this symmetry group is sufficient to remove the degeneracy in ^7F_J manifolds with only six nonzero B_q^k parameters. However, this widely used assumption of C_{2v} symmetry is invalid because molecular dynamics models of glasses[15] repeatedly show rare-earth sites have no symmetry (i.e., they have C_1 symmetry).

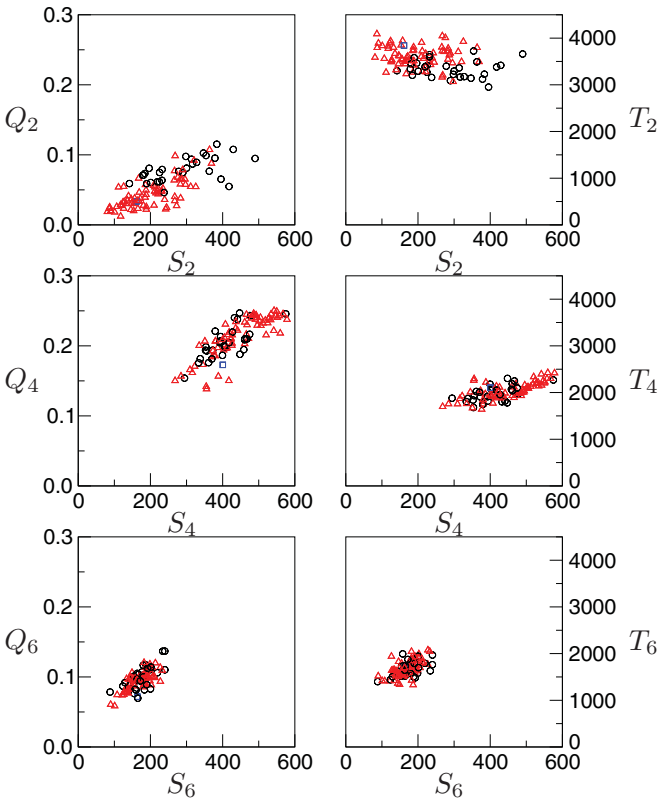

FIG. 16. (Color online) Contributions to the crystal-field strength components. Circles for CN = 5, triangles for CN = 6, and squares for CN = 7.

Since the choice of axes orientation cannot be significant for glasses, it is important to analyze the rotation-invariant crystal-field strength components S_k that are rotational invariants of B_q^k. In the previous Sec. V, a useful approximation was presented whereby S_k depends on separate functions of ligand distances, T_k, and ligand angular positions, Q_k, the latter being the rotation-invariant bond-orientational parameters.

Some additional comments can be made about the influence of coordination number (CN) on Q_k and T_k as shown in Fig. 16. For $k = 4$ and $k = 6$, there is no noticeable difference between rare-earth sites with CN = 5 (circles) and CN = 6 (triangles). For $k = 2$ it is seen that the T_2 values are slightly larger for CN = 6 (triangles) and slightly smaller for CN = 5 (circles). To understand the significance of CN in determining the values of T_k, we simplify the effect of ligand distance by assuming for a given Eu^{3+} ion all ligands have the same distance $R_j = R_{\rm avg}$ then

$$T_k \approx L\overline{B}_k \left(\frac{R_0}{R_{\rm avg}}\right)^{\tau_k}. \tag{42}$$

Increasing CN from 5 to 6 causes an increase in L that increases T_k. However, it also causes an increase in $R_{\rm avg}$ that decreases T_k due to the factor of $(\frac{R_0}{R_{\rm avg}})^{\tau_k}$. For T_4 and T_6, these factors cancel but for T_2 the increase due to L is dominant so T_2 values are slightly larger for CN = 6 and smaller for CN = 5.

Figure 16 shows there is also a strong influence from CN on Q_2, where values of Q_2 are significantly larger for CN = 5 (circles) and smaller for CN = 6 (triangles). This leads to S_2' and S_2 values being smaller for CN = 6 than CN = 5, as seen in Fig. 16 and Fig. 13, respectively. This effect of CN on Q_2 has been seen in previous studies[49,50] that used the rotation-invariant bond-orientational order parameters Q_k to study the local environments in disordered materials. Using sites based on trigonal bipyramid for CN = 5 and octahedra for CN = 6 it was seen that the values of Q_2 are nonzero for the former and zero for the latter. Instead, the values of Q_4 and Q_6 were nonzero for both CN = 5 and CN = 6.

Last, it is important to consider the possible implications for optimizing the luminescent properties of rare-earth-doped glasses. The present study has used Eu^{3+} ions as they make very convenient optical probes, with relatively simple sets of transitions. The results are expected to be transferable to other lanthanide ions, including Tb^{3+} and Er^{3+}, which are important for optical applications. The present study has shown for Eu^{3+} ions that the decrease in ground-state energy and the splitting of Stark levels, which produce inhomogeneous linewidth broadening, both occur in proportion to the crystal-field strength components S_k, and particularly S_2. Although the literature is scarce, it has been reported for Er^{3+} ions that the ground-state energy and the splitting of $I_{15/2}$ Stark levels are correlated, both in simulations[52] and FLN measurements.[53] Furthermore, it has been shown for lanthanide ions in general that the maximum splitting in Stark levels is proportional to the crystal-field strength S_{total}.[54] The remaining results of the present study should have general validity because they come from the mathematical properties of disordered structures: There is a dependence of S_2 on Q_2, Q_2 is larger for CN = 5 compared CN = 6, so the inhomogeneous linewidth broadening will be larger for rare-earth sites with CN = 5 compared to CN = 6.

It may be possible to control the inhomogeneous linewidth broadening by altering the glass composition so the local environment of rare-earth ions is biased toward a particular CN. In fact, previous studies of Q_k for different reference clusters suggest that Q_2 will be larger when CN is 5 or less, and Q_2 will be smaller when CN is 6 or higher.[50] Since Tb^{3+} and Er^{3+} ions are smaller than Eu^{3+} ions, they are likely have smaller CN than Eu^{3+}. This might mean it is more difficult to achieve CN = 6 for Tb^{3+} and Er^{3+} ions in silicate or oxide glasses. Larger rare-earth CN may be possible in nonoxide glasses, for example, a FLN study of fluorozirconate glasses assumed CN of 7 or 8.[55] Given the effect of CN on Q_2, structural characterization of the local environment of rare earths in glasses will remain important for efforts to reduce inhomogeneous linewidth broadening.

VII. CONCLUSION

A methodology has been demonstrated to calculate the optical spectra of rare-earth-doped glasses. A combination of features makes this methodology an improvement over previous work of this kind via the use of a superposition model to include covalent and overlap interactions, no use of higher symmetry than C_1, a realistic value for FWHM of 10 cm^{-1} for homogeneous broadening, inhomogeneous broadening solely due to the summation of contributions from all the Eu^{3+} ions, and a quantitative comparison with experimental oscillator strength in the absorption spectrum. Encouraging agreement is obtained between calculated and experimental spectra.

Subsequently, the relationship between transition energies and local environment of Eu^{3+} ions have been investigated in detail by studying the rotationally invariant crystal-field strength S_{total} and its components S_k. As seen in previous studies, the splitting of ^7F_J manifolds increases as the ground-state $^7F_0$ energy decreases and this is due to increasing mixing of $4f$ wave functions. These trends do follow the increase in S_{total} and show an approximately linear correlation with S_2.

Further analysis has examined rotation invariants of bond-orientational order parameters Q_k. The ligand distances and angular positions are seen to act independently in determining the values of S_4 which is primarily influenced by Q_4. For the important component S_2, the effect of ligand distances is roughly constant and Q_2 plays a major role in influencing the values of S_2. In fact, S_2 is noticeably related to coordination number where larger values of S_2 occur for CN = 5 than for CN = 6. This is a consequence of the properties of Q_2 that have previously been seen in studies of bond-orientational order in local environments of disordered materials. The detailed results presented here should prove helpful to glass scientists who want to better understand the link between local environment of rare-earth ions and inhomogeneous linewidth broadening in rare-earth-doped glasses.

ACKNOWLEDGMENTS

The work is supported by the UK Engineering and Physical Sciences Research Council (EPSRC). The authors are grateful to P. Strange for helpful discussions.

APPENDIX: SAMPLE PREPARATION AND SPECTROSCOPY MEASUREMENTS

Eu^{3+}-doped sodium silicate glasses of molar composition $33.8Na_2O \cdot 66SiO_2O \cdot 0.02Eu_2O_3$ and $33Na_2O \cdot 66SiO_2O \cdot 1Eu_2O_3$ were prepared by the melt-quench technique. Stoichiometric amounts of analytical grade Na_2CO_3 (Aldrich, 99.9%;), SiO_2 (Aldrich, 99.9%;), and Eu_2O_3 (Aldrich, 99.9%;) were thoroughly mixed in platinum crucible and melted in an electric furnace at 1300°C for 2 h in air. The melts were quenched by pouring onto a cold copper plate at room temperature and annealed for 2 h at 400°C under air atmosphere. The glasses were carefully polished for the spectroscopic measurements. Transparent glass samples of about $2 \times 2 \times 0.4$ cm^3 with excellent optical quality were obtained.

Room-temperature absorption spectra in the UV and visible regions were measured on careful polished glasses with a Varian Cary 5000 double beam spectrophotometer, using air as a reference. A spectral resolution of 1 nm was used. Room-temperature emission spectra and decay curves were measured using a tunable dye laser (Quanta System) operating with Exalite 395, pumped by the third harmonic (355 nm) of the fundamental radiation of a Quanta System pulsed Nd-YAG laser as the excitation source. The

emission radiation was collected using an optical fiber and dispersed with a Jobin-Yvon HR460 half-meter monochromator equipped with a 1200 lines/mm grating. The decay curves were measured with a Hamamatsu GaAs photomultiplier connected to a Le Croy Waverunner 500-MHz digital oscilloscope.

*Brunel Centre for Advanced Solidification Technology, Brunel University, Uxbridge UB8 3PH, United Kingdom.
†Computational Sciences, IBM Zurich Research Laboratory, Rüschlikon, Switzerland; Egypt Nanotechnology Research Centre, El-Sheikh Zayed City, Giza, Egypt.

[1]O. L. Malta and L. D. Carlos, Quim. Nova **26**, 889 (2003.
[2]S. Todoroki, K. Hirao, and N. Soga, J. Appl. Phys. **72**, 5853 (1992).
[3]D. Zhao, X. Qiao, X. Fan, and M. Wang, Physica B **395**, 10 (2007).
[4]G. Cormier, J. A. Capobianco, C. A. Morrison, and A. Monteil, Phys. Rev. B **48**, 16290 (1993).
[5]K. A. Gschneidner, L. Eyring, and M. B. Maple, *Handbook on the Physics and Chemistry of Rare Earths* (North-Holland, Amsterdam, 1978), Vol. 23.
[6]D. J. Newman and B. Ng, *Crystal Field Handbook* (Cambridge University Press, Cambridge, UK, 2000).
[7]D. J. Newman and B. Ng, Rep. Prog. Phys. **52**, 699 (1989).
[8]G. W. Burdick, C. K. Jayasankar, F. S. Richardson, and M. F. Reid, Phys. Rev. B **50**, 16309 (1994).
[9]G. Liu and B. Jacquier, *Spectroscopic Properties of Rare Earths in Optical Materials* (Springer, Berlin, 2005).
[10]D. K. T. Chan and M. F. Reid, J. Less-Common Met. **148**, 207 (1989).
[11]M. Fox, *Quantum Optics: An Introduction* (Oxford University Press, Oxford, UK, 2006).
[12]G. Cormier, J. A. Capobianco, and A. Monteil, J. Non-Cryst. Solids **152**, 225 (1993).
[13]R. N. Mead and G. Mountjoy, J. Phys. Chem. B **110**, 14273 (2006).
[14]G. Mountjoy, J. Non-Cryst. Solids **353**, 1849 (2007).
[15]N. D. Afify and G. Mountjoy, Phys. Rev. B **79**, 024202 (2009).
[16]W. Smith and T. R. Forester, J. Mol. Graphics **14**, 136 (1996).
[17]A. Pedone, G. Malavasi, M. C. Menziani, A. N. Cormack, and U. Segre, J. Phys. Chem. B **110**, 11780 (2006).
[18]P. P. Ewald, Ann. Phys. **369**, 253 (1921).
[19]M. P. Allen and D. J. Tildesley, *Computer Simulation of Liquids* (Clarendon Press, Oxford, UK, 1987).
[20]S. R. Elliott, *Physics of Amorphous Materials* (Longman, London, 1990).
[21]J. Jin, T. Yoko, F. Miyaji, S. Sakka, T. Fukunaga, and M. Misawa, J. Am. Ceram. Soc. **76**, 630 (1993).
[22]G. Mountjoy, Experimental Report 48219, Synchrotron Radiation Source, Daresbury Laboratory, UK (2008).
[23]W. T. Carnall, G. L. Goodman, K. Rajnak, and R. S. Rana, J. Chem. Phys. **90**, 3443 (1989).
[24]J. D. Jackson, *Classical Electrodynamics*, 3rd ed. (Wiley, New York, 1999).
[25]K. W. H. Stevens, Proc. Phys. Soc. A **65**, 209 (1952).
[26]B. G. Wybourne, *Spectroscopic Properties of Rare Earths* (Interscience, New York, 1965).
[27]S. Edvardsson and D. Åberg, Comput. Phys. Commun. **133**, 396 (2001).
[28]M. F. Reid, Program CFIT, University of Canterbury, Christchurch, New Zealand.
[29]M. F. Reid and F. S. Richardson, J. Chem. Phys. **79**, 5735 (1983).
[30]M. F. Reid and F. S. Richardson, J. Phys. Chem. **88**, 3579 (1984).
[31]J. D. Axe, J. Chem. Phys. **39**, 1154 (1963).
[32]B. R. Judd, Phys. Rev. **127**, 750 (1962).
[33]G. S. Ofelt, J. Chem. Phys. **37**, 511 (1962).
[34]R. C. Powell, *Physics of Solid-State Laser Materials* (AIP Press/Springer, New York, 1998).
[35]K. T. Greene and W. R. Morgan, J. Am. Ceram. Soc. **24**, 111 (1941).
[36]J. García Solé, L. E. Bausá, and D. Jaque, *An Introduction to the Optical Spectroscopy of Inorganic Solids* (Wiley, Hoboken, 2005).
[37]G. S. Dixon, R. C. Powell, and X. Gang, Phys. Rev. B **33**, 2713 (1986).
[38]G. Lei, J. E. Anderson, M. I. Buchwald, B. C. Edwards, and R. I. Epstein, Phys. Rev. B **57**, 7673 (1998).
[39]G. Tang, J. Zhu, Y. Zhu, and C. Bai, J. Alloys Compd. **453**, 487 (2008).
[40]W. T. Silfvast, *Laser Fundamentals*, 2nd ed. (Cambridge University Press, Cambridge, UK, 2004).
[41]M. H. V. Werts, R. T. F. Jukes, and J. W. Verhoeven, Phys. Chem. Chem. Phys. **4**, 542 (2002).
[42]N. S. Baek, Y. H. Kim, D. H. Lee, K. D. Seo, and H. K. Kim, Bull. Korean Chem. Soc. **30**, 1553 (2009).
[43]J. A. Capobianco, P. P. Proulx, M. Bettinelli, and F. Negrisolo, Phys. Rev. B **42**, 5936 (1990).
[44]H. Inoue, K. Soga, and A. Makishima, J. Non-Cryst. Solids **222**, 212 (1997).
[45]G. W. Burdick and M. F. Reid, Mol. Phys. **102**, 1141 (2004).
[46]R. P. Leavitt, J. Chem. Phys. **77**, 1661 (1982).
[47]Y. Y. Yeung and D. J. Newman, J. Chem. Phys. **82**, 3747 (1985).
[48]Y. Y. Yeung and D. J. Newman, J. Chem. Phys. **84**, 4470 (1986).
[49]P. J. Steinhardt, D. R. Nelson, and M. Ronchetti, Phys. Rev. B **28**, 784 (1983).
[50]A. Baranyai, A. Geiger, P. R. Gartrell-Mills, K. Heinzinger, R. McGreevy, G. Pálinkás, and I. Ruff, J. Chem. Soc., Faraday Trans. 2 **83**, 1335 (1987).
[51]R. A. Sack, J. Math. Phys. **5**, 245 (1964).
[52]H. Inoue, K. Soga, and A. Makishima, J. Non-Cryst. Solids **298**, 270 (2002).
[53]S. Zemon, G. Lambert, L. J. Andrews, W. J. Miniscalco, B. T. Hall, T. Wei, and R. C. Folweiler, J. Appl. Phys. **69**, 6799 (1991).
[54]F. Auzel and O. L. Malta, J. Phys. (France) **44**, 201 (1983).
[55]J. E. Munoz-Santiuste, U. R. Rodriguez-Mendoza, J. Gonzalez-Platas, and V. Lavin, J. Chem. Phys. **130**, 154501 (2009).